

Low pressure reversibly driving colossal barocaloric effect in two-dimensional vdW alkylammonium halides

Received: 30 August 2023

Accepted: 21 February 2024

Published online: 28 February 2024

Check for updates

Yi-Hong Gao^{1,2,8}, Dong-Hui Wang^{3,8}, Feng-Xia Hu^{1,2,4} ✉, Qing-Zhen Huang^{5,6}, You-Ting Song^{1,2}, Shuai-Kang Yuan^{1,2}, Zheng-Ying Tian^{1,2}, Bing-Jie Wang^{1,2}, Zi-Bing Yu^{1,2}, Hou-Bo Zhou^{1,2}, Yue Kan^{1,2}, Yuan Lin^{1,2}, Jing Wang^{1,2} ✉, Yun-liang Li^{1,2,4} ✉, Ying Liu³, Yun-Zhong Chen^{1,2} ✉, Ji-Rong Sun^{1,2,4}, Tong-Yun Zhao^{1,7} & Bao-Gen Shen^{1,2,5} ✉

Plastic crystals as barocaloric materials exhibit the large entropy change rivaling freon, however, the limited pressure-sensitivity and large hysteresis of phase transition hinder the colossal barocaloric effect accomplished reversibly at low pressure. Here we report reversible colossal barocaloric effect at low pressure in two-dimensional van-der-Waals alkylammonium halides. Via introducing long carbon chains in ammonium halide plastic crystals, two-dimensional structure forms in $(\text{CH}_3-(\text{CH}_2)_{n-1})_2\text{NH}_2\text{X}$ (X: halogen element) with weak interlayer van-der-Waals force, which dictates interlayer expansion as large as 13% and consequently volume change as much as 12% during phase transition. Such anisotropic expansion provides sufficient space for carbon chains to undergo dramatic conformation disordering, which induces colossal entropy change with large pressure-sensitivity and small hysteresis. The record reversible colossal barocaloric effect with entropy change $\Delta S_r \sim 400 \text{ J kg}^{-1} \text{ K}^{-1}$ at 0.08 GPa and adiabatic temperature change $\Delta T_r \sim 11 \text{ K}$ at 0.1 GPa highlights the design of novel barocaloric materials by engineering the dimensionality of plastic crystals.

On the continuous booming of resource-lack and environmental decay of global warming, the present cooling technique, mainly based on freon vapor compression system, needs to be substituted with efficient and zero-carbon emission cooling technique. Now leveraging the solid-state caloric effects for refrigeration has been intriguing alternative to conventional cooling technique, which takes advantages of zero direct carbon emission, high energy efficiency and susceptibility to integration¹. Caloric effects are exhibited in materials where phase transition with thermal change can be induced by external fields, such

as magnetic, electric and mechanical field. Specifically, the magnetic and electric fields can drive magnetocaloric and electrocaloric effect, respectively²⁻⁷. And the mechanical fields involving uniaxial stress and hydrostatic pressure drive elastocaloric^{8,9} and barocaloric effect respectively. The barocaloric cooling system superiorly features the accessible mechanical field, instead of costly magnetic field, and general barocaloric materials not requesting rigorous mechanical properties, which however is necessary for electrocaloric, magnetocaloric and elastocaloric materials^{10,11}. Escaping from the restriction of

¹Beijing National Laboratory for Condensed Matter Physics, Institute of Physics, Chinese Academy of Sciences, Beijing 100190, PR China. ²School of Physical Sciences, University of Chinese Academy of Sciences, Beijing 101408, PR China. ³College of Chemistry, Beijing Normal University, 100875 Beijing, PR China. ⁴Songshan Lake Materials Laboratory, Dongguan, Guangdong 523808, PR China. ⁵Ningbo Institute of Materials Technology & Engineering, Chinese Academy of Sciences, Ningbo, Zhejiang 315201, PR China. ⁶Spallation Neutron Source Science Center, Dongguan 523803, PR China. ⁷Ganjiang Innovation Academy, Chinese Academy of Sciences, Ganzhou, Jiangxi 341000, PR China. ⁸These authors contributed equally: Yi-Hong Gao, Dong-Hui Wang.

✉ e-mail: fxhu@iphy.ac.cn; wangjing@iphy.ac.cn; yunliangli@iphy.ac.cn; shenbg@iphy.ac.cn

mechanical property requirement and specific ferroicity such as ferromagnetism, ferroelectricity or ferroelasticity, barocaloric materials include a mass of structural phase change materials; developing from the incipient metallic compounds^{12–19}, some emergent barocaloric materials can exhibit colossal caloric effect^{20–29} with entropy change larger than $100 \text{ J kg}^{-1} \text{ K}^{-1}$, the phase transitions of which relate to the coupling between the remarkable structural change and large order-disorder transition of order parameters such as molecular orientation order^{20,21,23,25}, conformational order of organic chain^{27–29} and spin crossover²⁶.

Specifically, as a milestone in barocaloric cooling field, colossal caloric effect was achieved in polyalcohol plastic crystals²⁰, the entropy change during phase transition attaining from $384 \text{ J kg}^{-1} \text{ K}^{-1}$ in NPG ($(\text{CH}_3)_2\text{C}(\text{CH}_2\text{OH})_2$) to $682 \text{ J kg}^{-1} \text{ K}^{-1}$ in TRIS ($(\text{NH}_2)\text{C}(\text{CH}_2\text{OH})_3$), which approaches that of present freon refrigerant. However, the fatal low pressure-sensitivity and large hysteresis of phase transition (Table 1) bring about the irreversibility of caloric effect at low applying pressure, i.e., 0.1 GPa, in such three-dimension (3D) cubic plastic crystals, where the representative NPG exhibits none of reversible entropy change at pressure of 0.1 GPa. Underlyingly, the cubic plastic crystals maintain tight 3D structure via hydrogen bonds at ordered state³⁰, which limits the volume change also consequently pressure-sensitivity of phase transition. Meanwhile, large geometry incompatibility of two phases during phase transition related to the drastic symmetry breaking/restoration of lattice tends to cause large hysteresis^{31–33}. Therefore, it is crucial to regulate comprehensively the entropy change, pressure sensitivity and hysteresis of phase transition, for achieving the reversible colossal barocaloric effect (BCE) driven by low pressure. It remains a challenge for BCE to enhance the reversibility while maintaining the magnitude as large as polyalcohol plastic crystals.

Here, we demonstrate that by introducing the alkyl chains in ammonium halide plastic crystal and constructing the two-dimensional (2D) van-der-Waals (vdW) alkylammonium halides, the colossal BCE with entropy change $\sim 400 \text{ J kg}^{-1} \text{ K}^{-1}$ can be reversibly driven by pressure lower than 0.1 GPa. Single crystal x-ray diffraction (SC-XRD) indicated that long organic chains are assigned parallelly and anchored at the both ends of N–Cl plane to form the 2D structure in

didecyl ammonium chloride ($(\text{CH}_3-(\text{CH}_2)_9)_2\text{NH}_2\text{Cl}$) (Fig. 1a). Within the 2D layered system maintained by intralayer N–H...Cl hydrogen bond and interlayer vdW interactions, the structural change across phase transition and relevant dynamics at molecular level were revealed by powder x-ray diffraction (PXRD), molecular dynamics (MD) simulation and temperature-variable infrared (IR) spectroscopy.

Our results demonstrated that the 2D $(\text{CH}_3-(\text{CH}_2)_9)_2\text{NH}_2\text{Cl}$ undergoes interlayer expansion as large as 13% along the length direction of carbon chains (*c* axis) while *ab* plane remains nearly unchanged, consequently volume expansion as much as 12% occurs during phase transition. Such anisotropic expansion of lattice provides sufficient space for carbon chains to undergo dramatic conformation disordering, which induces colossal entropy change with large pressure-sensitivity and small hysteresis. MD simulation elucidated the specific disordering process from perspective of radial distribution function *g*(*r*) and dihedral angle of carbon chains, and the measured IR spectra gave fingerprint information across phase transition for each component, i.e., the NH_2^+ and N–H...Cl hydrogen bonds, the CH_2 and C–C chains, and the CH_3 tails, in the entire $(\text{CH}_3-(\text{CH}_2)_9)_2\text{NH}_2^+$ chains. The peculiar dynamics enables realization of colossal entropy change from disordering of organic chains, high sensitivity to pressure from large volume expansion, and relatively low hysteresis stemming from the low-dimension structure related low energy barrier of phase transition, thus accomplishing the record reversible colossal barocaloric entropy change $\Delta S_r \sim 400 \text{ J kg}^{-1} \text{ K}^{-1}$ at 0.08 GPa in $(\text{CH}_3-(\text{CH}_2)_9)_2\text{NH}_2\text{Cl}$ affirmed by pressure differential scanning calorimetry. In addition, adiabatic temperature change ΔT_{ad} as large as 11 K at applying pressure of 0.1 GPa was demonstrated by direct barocaloric measurement. These performances exceed those of all other barocaloric materials reported to date (Table 1).

Results

2D vdW crystalline structure and thermal properties of phase transition

The dialkyl ammonium halides $(\text{CH}_3-(\text{CH}_2)_{n-1})_2\text{NH}_2\text{X}$ (X: halogen element) evolve from the substitution of two alkyl chains $(\text{CH}_3-(\text{CH}_2)_{n-1})$ for two hydrogen atoms in ammonium halide molecule, in such process,

Table 1 | Comparisons of colossal barocaloric materials with solid-solid phase transition exhibiting entropy change larger than $100 \text{ J kg}^{-1} \text{ K}^{-1}$

Compounds	T_s (K)	$ \Delta S $ ($\text{J kg}^{-1} \text{ K}^{-1}$)	Hys. (K) T rate (K min^{-1})	dT_s/dP (K GPa^{-1})	ΔV ($\text{E-5 m}^3 \text{ kg}^{-1}$)	$ \Delta S_p _{-0.1 \text{ GPa}}$ ($\text{J kg}^{-1} \text{ K}^{-1}$)	$ \Delta S_r _{-0.1 \text{ GPa}}$ ($\text{J kg}^{-1} \text{ K}^{-1}$)	Refs.
dC_{10}Cl	325	400	8 (1)	190	11.9	400	400	This work
NPG $(\text{CH}_3)_2\text{C}(\text{CH}_2\text{OH})_2$	313	384	14 (0.1)	133	4.6	0	0	20,21
PG $(\text{CH}_3)\text{C}(\text{CH}_2\text{OH})_3$	354	485	4 (2–4)	79	5.1	445	155	23,55
TRIS $(\text{NH}_2)\text{C}(\text{CH}_2\text{OH})_3$	407	682	75 (2–4)	37	3.7	0	0	23,56
AMP $(\text{NH}_2)(\text{CH}_3)\text{C}(\text{CH}_2\text{OH})_2$	353	632	-	64	4.6	0	0	23,55
NPA $(\text{CH}_3)_3\text{C}(\text{CH}_2\text{OH})$	232	204	20 (2–4)	220	-	0	0	23
1-Cl-ada	254	132	9 (2–4)	270	4.7	170	160	25
1-Br-ada	308	102	9 (2.5–3)	333	4	150	135	25
1-adamantanol	361	210	15	179	4.5	-250	0	57
2-methyl-2-adamantanol	375	371	11	241	8.8	-380	-350	57
CaF_2	1400	226	-	-	-	-	-	22
$(\text{CH}_3-(\text{CH}_2)_8-\text{NH}_3)_2\text{MnCl}_4$	294	212	5.2 (1)	172	-	212	212	28
$(\text{CH}_3-(\text{CH}_2)_9-\text{NH}_3)_2\text{MnCl}_4$	312	230	4.0 (1)	150	-	230	230	28
PEG10000/PET15000	334	426	21.8 (1)	97	-	416	35.6	58
NH_4SCN	364	129	~25	300	-3.8	129	-100	59

Parameters are listed containing the phase transition temperature during heating (T_s), entropy change during phase transition at atmosphere pressure ($|\Delta S|$), hysteresis (Hys.), the dependence of T_s on pressure (dT_s/dP), volume change of phase transition from experiment (ΔV), barocaloric entropy change induced by 0.1 GPa ($|\Delta S_p|_{-0.1 \text{ GPa}}$) and reversible barocaloric entropy change induced by 0.1 GPa ($|\Delta S_r|_{-0.1 \text{ GPa}}$). The ones from NPG to 2-methyl-2-adamantanol on the upper part denote 3D plastic crystals.

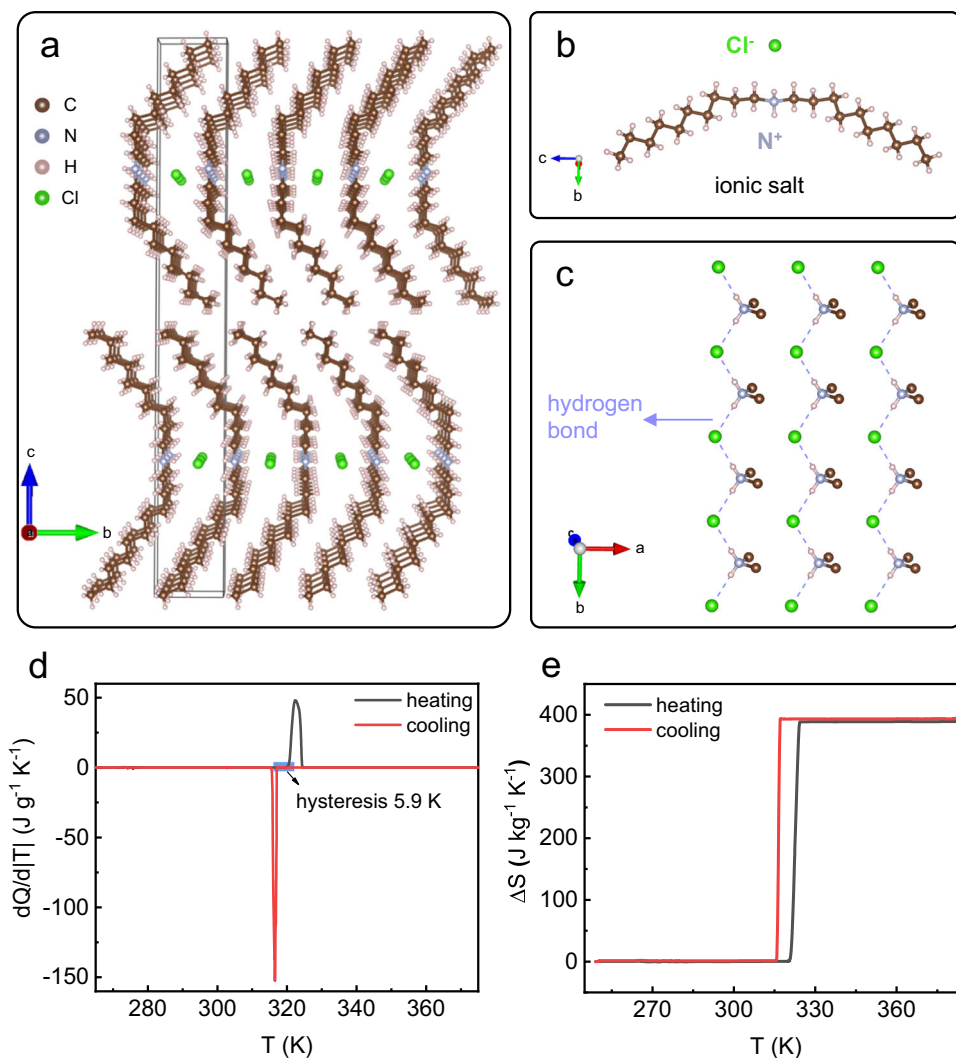


Fig. 1 | Crystalline structure and thermal properties of phase transition for $(\text{CH}_3-(\text{CH}_2)_9)_2\text{NH}_2\text{Cl}$. **a** Crystalline structure of $(\text{CH}_3-(\text{CH}_2)_9)_2\text{NH}_2\text{Cl}$ at 300 K, where the unit cell is marked by black frame. **b** Molecular structure of $(\text{CH}_3-(\text{CH}_2)_9)_2\text{NH}_2\text{Cl}$. **c** N-H...Cl hydrogen bond interaction in

$(\text{CH}_3-(\text{CH}_2)_9)_2\text{NH}_2\text{Cl}$, where partial carbon and hydrogen atoms are omitted. **d** DSC measurement of $(\text{CH}_3-(\text{CH}_2)_9)_2\text{NH}_2\text{Cl}$ at atmosphere pressure with temperature ramping rate 0.1 K min^{-1} . **e** Temperature-dependence of entropy change across phase transition calculated from **(d)**.

introducing cylindrical long chains in ammonium halide of trivial plastic crystal formed by globular species generates the novel crystal system^{34–39}. We successfully synthesized $(\text{CH}_3-(\text{CH}_2)_{n-1})_2\text{NH}_2\text{X}$ ($n = 6, 8, 10$; $\text{X} = \text{Cl}, \text{Br}$) materials and single crystals for the first time. As our measurements show (Supplementary Table 1), solid-solid first-order phase transitions were affirmed by differential scanning calorimetry (DSC) at atmospheric pressure, intriguingly the thermal effect presented sizably and tunably. After cultivating high-quality single crystals of $(\text{CH}_3-(\text{CH}_2)_9)_2\text{NH}_2\text{Cl}$ (abbreviated as dC_{10}Cl) and $(\text{CH}_3-(\text{CH}_2)_9)_2\text{NH}_2\text{Br}$ (abbreviated as dC_{10}Br), SC-XRD under atmospheric pressure was performed and ordered crystalline state with emerged 2D layered structure was demonstrated at room temperature. Considering the remarkable thermal effect of phase transition and the transition temperature closer to room temperature, dC_{10}Cl is chosen for elucidation of 2D vdW structure and further exploration.

The crystal structure of dC_{10}Cl at room temperature is presented in Fig. 1a. The dC_{10}Cl molecules are packed with a triclinic crystal lattice, two molecules in each lattice (Supplementary Figs. S3, S4 and Table S2), and the lattice is parameterized with $a = 4.9 \text{ \AA}$, $b = 5.3 \text{ \AA}$, $c = 43.2 \text{ \AA}$, $\alpha = 89.6^\circ$, $\beta = 89.7^\circ$ and $\gamma = 88^\circ$. As Fig. 1a shows, $((\text{CH}_3-(\text{CH}_2)_9)_2\text{NH}_2)^+$ alkylammonium cations and Cl^- anions, constituting the dC_{10}Cl molecules, are assigned orderly to form the

layered structure, and the specific conformer of alkylammonium species is presented in Fig. 1b, where nitrogen atom (N^+) of positive charge center is bonded with two hydrogen atoms and two long decyl chains ($\text{CH}_3-(\text{CH}_2)_9$). Concretely, within each molecule layer of dC_{10}Cl , the nitrogen atoms (N^+) locate at the center of $(\text{CH}_3-(\text{CH}_2)_9)_2\text{NH}_2^+$ and chlorine atoms (Cl^-) are spread in ab plane, as shown in Fig. 1c, while $(\text{CH}_3-(\text{CH}_2)_9)$ chains, parallel to each other, are extended along the direction nearly perpendicular to the ab plane. Wherein, the N-H...Cl hydrogen bond interaction zigzag along the b axis (Fig. 1c), electrostatic interaction between N^+ and Cl^- , and lateral vdW force in the ab plane between the hydrocarbon chains are accountable for the intralayer interaction. Moreover, between the molecular layers, vertical vdW force along the c axis through the CH_3 groups at the end of $(\text{CH}_3-(\text{CH}_2)_9)$ chains maintain the structural stability (Fig. 1a). Therefore, the 2D layered structure is constructed by anisotropic interaction for intralayer and interlayer direction in dC_{10}Cl , dominantly strong intralayer ionic interaction and hydrogen bond interaction and weak interlayer vdW interaction.

The significant thermal effect of phase transition in dC_{10}Cl was further revealed by microcalorimetry performed on dC_{10}Cl single crystal at temperature changing rate of 0.1 K min^{-1} . As shown in Fig. 1d, a sharp first-order phase transition emerges at around $T_s \sim 320 \text{ K}$, with

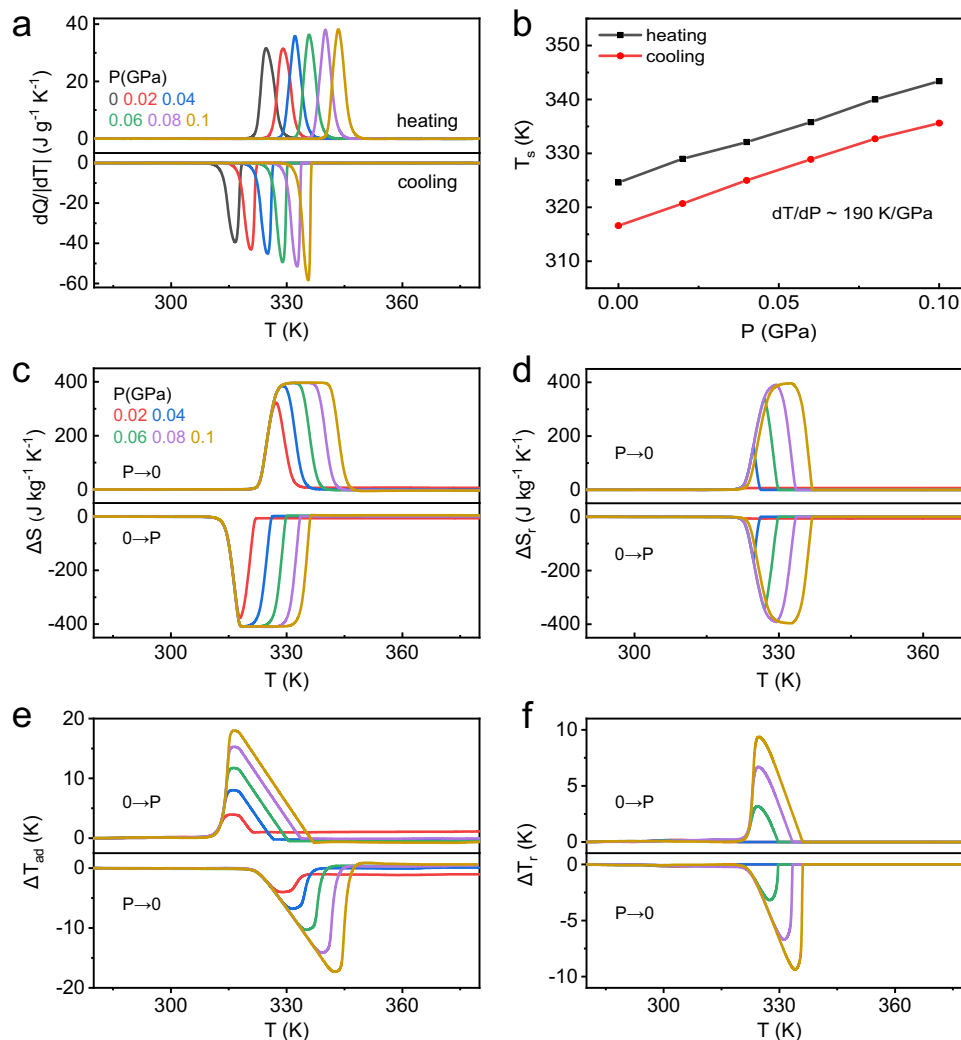


Fig. 2 | Barocaloric performance of $(\text{CH}_3-(\text{CH}_2)_9)_2\text{NH}_2\text{Cl}$ obtained by the quasi-direct method. **a Heat flow curves under variable pressure measured at a temperature rate 1 K/min. **b** Pressure-dependent phase transition temperature from (a). **c** Isothermal entropy change ΔS at variable pressure from the pressure-variable entropy curves (Supplementary Fig. S5). **d** Reversible entropy change ΔS_r , by**

overlapping of pressurization and depressurization from (c). **e** Adiabatic temperature change ΔT_{ad} from pressure-variable entropy curves (Supplementary Fig. S7). **f** Reversible adiabatic temperature change ΔT_r from heating entropy curve at atmosphere pressure and cooling entropy curves under applied pressure.

a low thermal hysteresis of 5.9 K determined as the distance between endothermic and exothermic peaks. The entropy change of phase transition (Fig. 1e), calculated by the integration of heat flow curves in Fig. 1d, attains $-400 \text{ J kg}^{-1} \text{ K}^{-1}$, which indicates the colossal caloric effect in 2D alkylammonium halide system analogous to that in 3D polyalcohol plastic crystals^{20,23}. Also, the thermal behavior of phase transition for dC_{10}Cl single crystal, i.e., transition temperature, entropy change and thermal hysteresis, is almost identical to that of polycrystal counterparts (Supplementary Table S1). The coexistence of large entropy change and low hysteresis in such 2D alkylammonium halide meets the prerequisite of colossal reversible BCE at low pressure, which is urgently attractive to be verified further.

Barocaloric performances

To investigate the barocaloric character of dC_{10}Cl , the pressure differential scanning calorimetry (P-DSC) was used to acquire the thermal behavior of phase transition under applied pressures and quasi-directly reveal the pressure-induced caloric effect. As shown in Fig. 2a, under stable applied pressure, the sample exhibits phase transition-related thermal response on heating and cooling with the rate of 1 K min^{-1} (noted that the hysteresis can be larger for higher temperature scanning rates, which could critically influence the reversibility of the BCE

depending on the operation conditions; specific analysis can be seen in Supplementary Note 2). In the pressure range of 0–0.1 GPa, the transition temperature T_s rises linearly with the applied pressure, exhibiting a magnificent rate of 190 K GPa^{-1} . The phase diagram of dC_{10}Cl in Fig. 2b exhibits the identically high sensitivity to pressure for endothermic and exothermic peaks, and consequently consistent thermal hysteresis of $\sim 8 \text{ K}$ under variable pressures. Also, identical entropy changes of phase transition under different pressures are revealed as $-400 \text{ J kg}^{-1} \text{ K}^{-1}$ (Supplementary Fig. S5). Including the entropy change from specific heat outside the phase transition region (Supplementary Fig. S6), the total entropy curves were constructed under variable pressures (Supplementary Fig. S7), on basis of which the pressure-induced isothermal entropy change (ΔS) and adiabatic temperature change (ΔT_{ad}) can be calculated quasi-directly. As shown in Fig. 2c, ΔS induced by pressure of 0.02 GPa reaches $332 \text{ J kg}^{-1} \text{ K}^{-1}$, and the maximum ΔS of $-400 \text{ J kg}^{-1} \text{ K}^{-1}$ can be realized by applying 0.06 GPa, which represents colossal barocaloric entropy change under low pressure. The colossal BCE is further evidenced by large ΔT_{ad} , as shown in Fig. 2e, ΔT_{ad} as large as 18 K is induced by a pressure of 0.1 GPa.

Furthermore, to evaluate the barocaloric effect in thermodynamic cycle of practical significance, the reversible entropy change (ΔS_r) and reversible adiabatic temperature change (ΔT_r) were obtained quasi-

directly as Fig. 2d, f, respectively. The maximum ΔS_r of $\sim 400 \text{ J kg}^{-1} \text{ K}^{-1}$ can be implemented under 0.08 GPa, which manifests that the complete phase transition of $dC_{10}Cl$ can be reversibly driven by a low pressure of 0.08 GPa; for reversible ΔT_r induced by pressure (Fig. 2f), the maximum reaches 9.4 K at 0.1 GPa. Overall, due to the coexistence of large entropy change, high pressure-sensitivity, and low hysteresis of

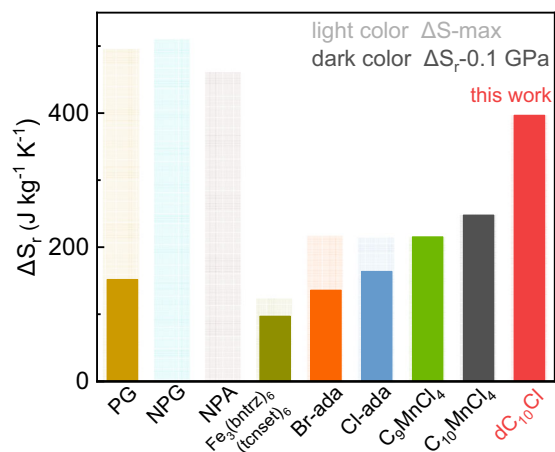


Fig. 3 | The comparison of reversible barocaloric entropy change of our $dC_{10}Cl$ with other reported colossal barocaloric materials. The materials include 3D plastic crystals PG, NPG, NPA, spin-crossover $Fe_3(bntrz)_6(tcnsct)_6$, substituted adamantane Br-adamantane, Cl-adamantane and hybrid organic-inorganic perovskite $(C_nH_{2n+1}NH_3)_2MnCl_4$ ($n = 9, 10$)^{20,21,23,25–29}. Light color denotes the entropy change ΔS_r of phase transition, while dark color marks the reversible entropy change ΔS_r driven by a hydrostatic pressure of 0.1 GPa.

phase transition in $dC_{10}Cl$, the colossal reversible BCE under pressure as low as 0.1 GPa can be achieved. As shown in Fig. 3 and Table 1, the 2D $dC_{10}Cl$ exhibits prominent phase transition with caloric effect as large as 3D plastic crystal polyalcohol (PG, NPG and NPA), but significantly the phase transition can be driven reversibly and completely by a low pressure of 0.1 GPa to induce the maximum entropy change. As a result, the reversible colossal caloric effect at 0.1 GPa exceeds that of all other reported barocaloric materials containing 3D plastic crystals, spin-crossover complex and hybrid organic-inorganic perovskites^{20,21,23,25–29}.

Moreover, the direct measurement (schematically in Fig. 4d) of reversible BCE was performed on $dC_{10}Cl$. The pressurization and depressurization processes are accomplished within 3 s, so the sample temperature was detected almost adiabatically. As shown in Fig. 4a, at $\sim 330 \text{ K}$, the reversible adiabatic temperature change (ΔT_r) of $\sim 11 \text{ K}$ can be induced by a pressure of 0.1 GPa, which is affirmed by cycle test of pressurization and depressurization (Fig. 4c). Noticeably, the ideal adiabatic cycle comprises the pressurization-induced temperature-increase ($T_0 \rightarrow T_1$) and depressurization-induced temperature-decrease ($T_1 \rightarrow T_0$). However, we failed to accurately measure the temperature change in the depressurization process since the applied pressure cannot be fully maintained but spontaneously release some due to our device. Concretely in Fig. 4a and contrastive illustration in Fig. 4b, the temperature change in the first process (I) reflects the thermal effect induced by approximately adiabatically pressurization to 0.1 GPa, and in the second process (II) involving the spontaneous release of pressure, the heat exchange between the heated sample and environment with temperature of $\sim 330 \text{ K}$ contributes to the cooling trend; additionally in the third process (III), at initial temperature of $\sim 330 \text{ K}$, $\Delta T_{ad} \sim 6 \text{ K}$ can be induced by depressurization where the ΔT_{ad} is underestimated due to the spontaneous release of pressure in the second process (II), and similar to the second process (II), heat

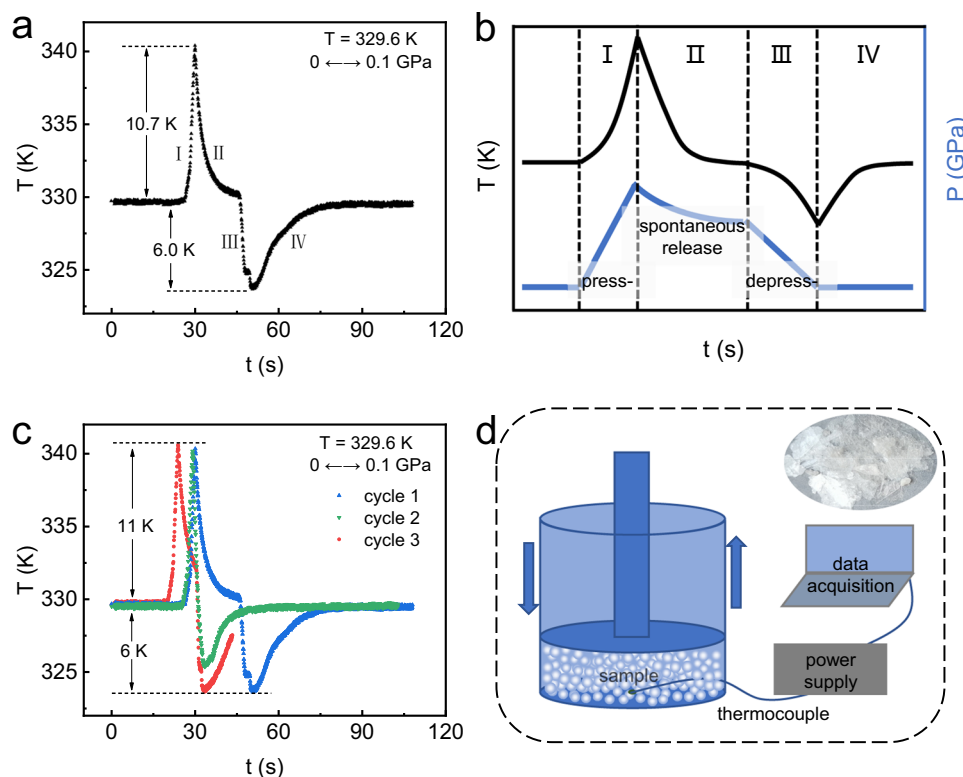


Fig. 4 | The direct measurement of adiabatic temperature change ΔT_{ad} driven by pressure in $dC_{10}Cl$. **a** ΔT_{ad} induced by pressure of 0.1 GPa. **b** Schematic illustration of temperature change and pressure evolution during the adiabatic test, containing the processes of pressurization (press-) and depressurization (depress-).

c Cycle measurements of ΔT_{ad} induced by pressure of 0.1 GPa. **d** Schematic diagram of direct measurement of ΔT_{ad} , where the sample's image is for indication only, and the real image of single crystal sample is shown at top right.

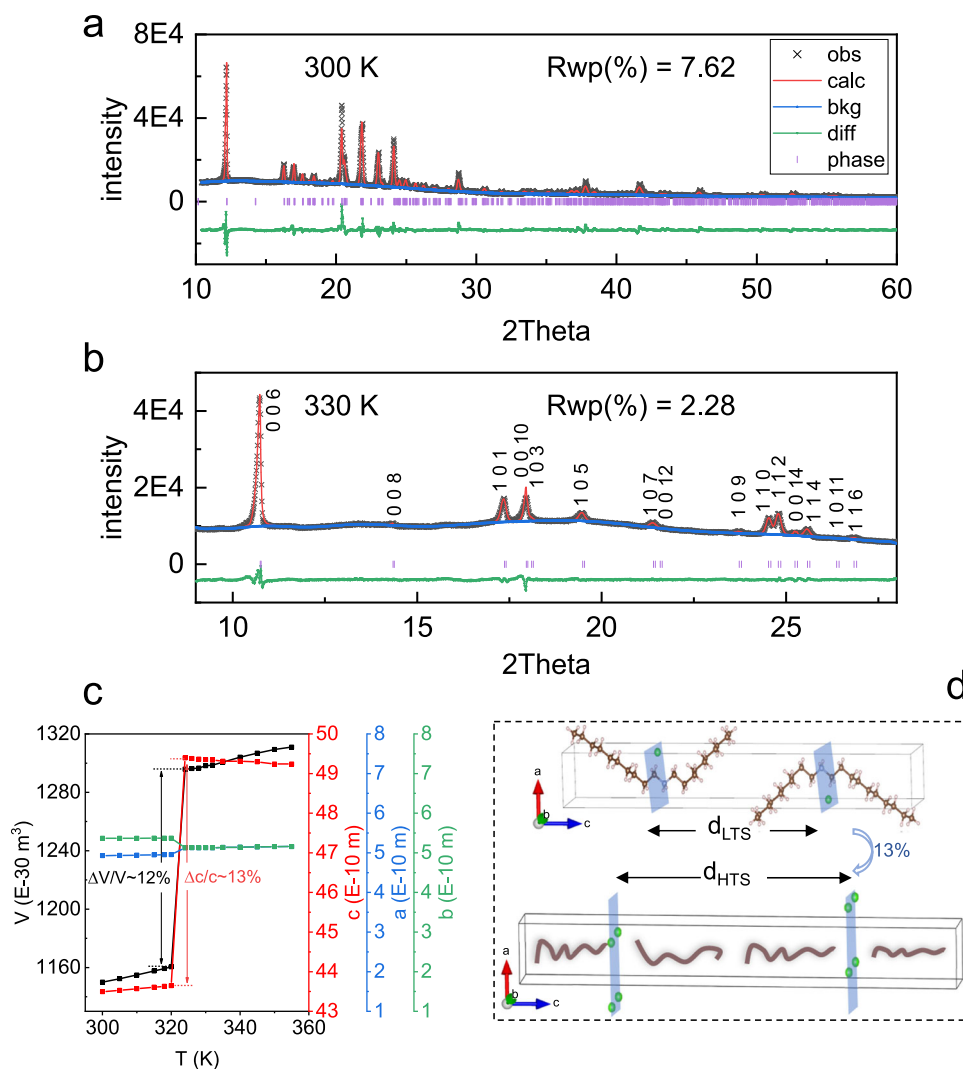


Fig. 5 | Powder x-ray diffraction result of the $(\text{CH}_3-(\text{CH}_2)_9)_2\text{NH}_2\text{Cl}$. **a** Refinement result of diffraction pattern at 300 K for low-temperature-state in $(\text{CH}_3-(\text{CH}_2)_9)_2\text{NH}_2\text{Cl}$. **b** Le Bail method fitting result of diffraction pattern at 330 K for high-temperature-state in $(\text{CH}_3-(\text{CH}_2)_9)_2\text{NH}_2\text{Cl}$, where the observed (black), calculated patterns (red), their difference (green), peak positions (purple bar),

background (blue), and error factor Rwp are provided. **c** The evolution of lattice parameters and unit cell volume with temperature in $(\text{CH}_3-(\text{CH}_2)_9)_2\text{NH}_2\text{Cl}$. **d** Schematic illustration of layer spacing expansion across the phase transition in $(\text{CH}_3-(\text{CH}_2)_9)_2\text{NH}_2\text{Cl}$.

exchange between the sample and environment causes temperature rising back during the fourth process (IV). However, the good repeatability on pressurization during cycle test demonstrates the reliability of measured ΔT_r (Fig. 4c).

Moreover, larger ΔT_r of ~ 22 K can be achieved under pressure of 0.2 GPa at 330 K (Supplementary Fig. S9), but further enlarging applied pressure as 0.3 GPa cannot enhance the ΔT_r any more (Supplementary Fig. S10), indicating the maximum of adiabatic temperature change in dC_{10}Cl is ~ 22 K. The superior ΔT_r at low pressure can be revealed by comparing the dC_{10}Cl with all the reported materials measured by direct measurement method (Supplementary Fig. S11). Hitherto the colossal reversible barocaloric effect of 2D alkylammonium halide dC_{10}Cl has been evidenced by both quasi-direct and direct measurements, and the underlying mechanism of intriguing phase transition will be discussed further.

Structural transition

From SC-XRD, although the structure was detailed at 300 K below transition temperature $T_s \sim 320$ K for dC_{10}Cl , we were unable to obtain regular diffraction information via SC-XRD at above T_s though a partial stacking order remains (Supplementary Fig. S2). To disclose the

structural evolution of 2D vdW alkylammonium halide dC_{10}Cl across T_s , the temperature-variable PXRD under atmospheric pressure was performed on dC_{10}Cl at 300–355 K. And the resulted diffraction patterns (Supplementary Fig. S12) show that dC_{10}Cl exhibits a transition onset of lattice symmetry at 322 K, then the phase transition gets accomplished at 324 K, which is in perfect accordance with the results from DSC characterization above. Further Rietveld refinement of diffraction patterns (Supplementary Figs. S13–17) demonstrates that at low-temperature-state (LTS) below 322 K, dC_{10}Cl maintains the triclinic lattice with space group of P-1, specifically $a = 4.9$ Å, $b = 5.4$ Å, $c = 43.5$ Å, $\alpha = 90^\circ$, $\beta = 89.8^\circ$ and $\gamma = 88.2^\circ$ at 300 K ($a = 4.9$ Å, $b = 5.3$ Å, $c = 43.2$ Å, $\alpha = 89.6^\circ$, $\beta = 89.7^\circ$ and $\gamma = 88^\circ$ from SC-XRD, 300 K), where the carbon chains present definite conformer (Fig. 5a). Such refined molecular configuration of dC_{10}Cl at 300 K from PXRD fits well with the result resolved from SC-XRD patterns (Supplementary Table S6).

For the high-temperature-state (HTS) higher than 324 K, although the organic chains become disordering and lose translational symmetry with definite atomic position, the crystalline structure composed of inorganic Cl ions can be confirmed by Le Bail method (Supplementary Figs. S18–26, Fig. 5d), where reliable lattice parameters can be obtained before detailed atomic position fitting⁴⁰. As

shown in Fig. 5b, the lattice at HTS, at 330 K for instance, is body-centered tetragonal, presenting space group of $I4/mmm$ for instance, according to the observed reflection peaks with the even sum of h , k , and l induced by extinction rule of body-centered space group. Specifically, the tetragonal lattice at 330 K is parameterized with $a = b = 5.13 \text{ \AA}$ and $c = 49.35 \text{ \AA}$. It should be noted that the carbon chains would exhibit multiple variable conformations, while the Cl^- anions become less bonded by the organic chains (see IR spectra below). Hence it is understandable that the crystalline structure composed of inorganic Cl^- ions adapts the higher symmetry at HTS time-averagely and space-averagely, wherein the Cl^- anions can be easily accommodated in the high symmetry lattice (schematically in Fig. 5d).

From the refined lattice information, it is revealed that the interlayer expansion along c axis can be as large as 13% across T_s (as shown in Fig. 5c and illustrative transition from d_{LTS} to d_{HTS} in Fig. 5d), while ab plane remains nearly unchanged ($4.9 \text{ \AA} \times 5.3 \text{ \AA}$ at LTS (300 K), $5.13 \text{ \AA} \times 5.13 \text{ \AA}$ at HTS (330 K)), consequently volume expansion as much as 12% ($\Delta V \sim 11.9 \text{ E-5 m}^3 \text{ kg}^{-1}$) occurs during phase transition (Fig. 5c). The specific anisotropic expansion can be ascribed to the layered 2D structural character in dC_{10}Cl ; within the 2D structure, the weak interlayer vdW interaction along c axis dominantly contributes to the prominent expansion across the phase transition.

From the underlying relationship between the volume change and thermal effect of phase transition, such an extraordinary large expansion along the length direction of carbon chains (Fig. 5d) can endow sufficient free volume for carbon chains between N-Cl planes, potentially allowing for great conformational disorder of carbon chains and consequently large entropy change in dC_{10}Cl . And the interlayer spacing enlargement-induced volume change of phase transition in dC_{10}Cl is shown to be largest among the colossal barocaloric materials (Table 1). Based on the Clausius-Clapeyron relation ($dT_s/dP = \Delta V/\Delta S$), the large entropy change across the phase transition tends to induce the low pressure-sensitivity of phase transition. Significantly, in the 2D vdW dC_{10}Cl , the volume change of phase transition appears to be colossal, due to the weak interlayer vdW interaction. In this case, the large pressure sensitivity of phase transition with colossal entropy change can be accomplished with the compensation of the large volume expansion. Therefore, the coexistence of colossal entropy change and magnificent volume change during the phase transition contributes to the superior BCE reversibly driven by low pressure in 2D vdW alkylammonium halide system dC_{10}Cl . The conformational dynamics of carbon chains during phase transition in dC_{10}Cl is intriguing to be explored, for elaborating the mechanism of peculiar phase transition therein.

Molecular dynamics simulation

Molecular dynamics (MD) simulation was performed on dC_{10}Cl to clarify the conformational evolution of organic chains, which is generally difficult to be detected experimentally for the intricacy of organic chain conformations at HTS. Based on the molecular structure parameters from SC-XRD at 300 K, we constructed supercell and performed MD simulations. See details in Methods.

As shown in Supplementary Fig. S27, a first-order phase transition was deduced by MD simulation at $\sim 430 \text{ K}$ in dC_{10}Cl , where the over-estimated transition temperature can be attributed to the superheating problem in MD simulations, i.e., the perfect crystal without surfaces and defects in simulation contrary to the real materials where phase transition onset could be at surfaces and defects⁴¹. Concretely at simulated LTS (Fig. 6a), the molecules stay aligned regularly and organic chains keep uniform conformation. Contrastingly at simulated HTS (Fig. 6b), the conformation of organic chains become disordered prominently, also the Cl^- anions bear positional disorder arising from the intensified vibration.

The conformational transition of organic chains can be illustrated quantitatively by the statistical result of radial distribution function (Fig. 6c, d) and dihedral angle distribution (Fig. 7). Radial distribution function $g(r)$ refers to the variation of atomic density as a function of distance from a reference atom (as schematically shown in Fig. 6e); it is an indication of atomic packing pattern⁴². The temperature-variable $g(r)$ of carbon atoms in dC_{10}Cl are shown in Fig. 6c, the trend of $g(r)$ at simulated LTS (300 K and 400 K) differing from that at simulated HTS (500 K and 600 K). For the atomic distance of 0–5 \AA , $g(r)$ presents multiple sharp peaks at LTS, where each peak (p_1 – p_4 in Fig. 6c) refers to each radial distance between carbon atoms in carbon chains with short-range ordered *trans* conformer (Fig. 6e). Across the LTS–HTS transition, the p_4 peak in $g(r)$ tends to disappear, indicating the conformal disordering of C–C–C–C group with 4 C–C bonds, while partially ordered C–C–C–C with 3 C–C bonds still exists at HTS. For the range of 5–20 \AA (Fig. 6f), $g(r)$ presents multiple peaks at LTS while getting flat after the phase transition, which manifests the carbon chains transform from the long-range ordered conformer chains aligned regularly to the disordered conformer chains without regular arrangement⁴³; Fig. 6f schematically represents that the conformational transition of carbon chains during phase transition gives rise to the distribution disorder of interchain and intrachain carbon atoms, consequently rendering the radial distance getting uniform at HTS.

More explicit demonstration of carbon chain conformer evolution during the phase transition can be given by temperature-variable C–C–C–C dihedral angle composed of 3 C–C bonds (Fig. 7). The C–C–C–C dihedral angle refers to the angle between the plane formed by the first two C–C bonds and the plane formed by the last two C–C bonds, thus indicative of the local conformer of C–C–C–C group. Specifically, the *trans* conformer exhibits the dihedral angle of around 180° , while the rotation of partial chain around the carbon bonds induces the appearance of various chain conformation and dihedral angles, as schematically shown in Fig. 7b. In Fig. 7a, the C–C–C–C dihedral distributions at different temperatures reveal the distinguishable motifs of C–C–C–C dihedral angles before and after the phase transition. At LTS, the bands concentrate around 160° – 180° and 60° – 90° , where the former denotes *trans*-like conformer and the latter denotes the *gauche* conformer in carbon chains. In accordance with the SC-XRD result, the N–H...Cl hydrogen bond interaction between the $((\text{CH}_3-(\text{CH}_2)_9)_2\text{NH}_2)^+$ group and Cl^- anions induces the *gauche* conformer of C–C–C–C closest to the Cl framework, and others are still in *trans* (see Fig. 1b). At HTS, more C–C–C–C dihedral angles are concentrated around 60° – 90° , while there are less for 160° – 180° ; except the two categories, other angles emerge at HTS, which denotes the transient state during the dynamic *trans-gauche* conformer transition. The dispersive C–C–C–C dihedral angles at the HTS manifests the multiplying conformers coexisted in carbon chains, which refers to the specific disorder of organic chains in dC_{10}Cl .

The conformation disordering of organic chains related to the free twisting at carbon chains gives rise to the colossal entropy change during the order–disorder phase transition^{27–29,44}, which accounts for the large entropy change in dC_{10}Cl . Moreover, the enthalpy change of phase transition per mole for dC_{10}Cl approaches double that for *n*-decane (Supplementary Table S7), which indicates the disordering of organic chains is analogous to the incomplete melting-like free twisting and conformation disorder of organic chains.

Molecular infrared vibration

To investigate the interaction evolution at the level of atomic group during the phase transition, the molecular infrared vibration behaviors before and after the phase transition were explored (Fig. 8). We measured the temperature-variable infrared spectra in the wavenumber range of 900–4000 cm^{-1} from 295 K to 353 K on heating. The change of

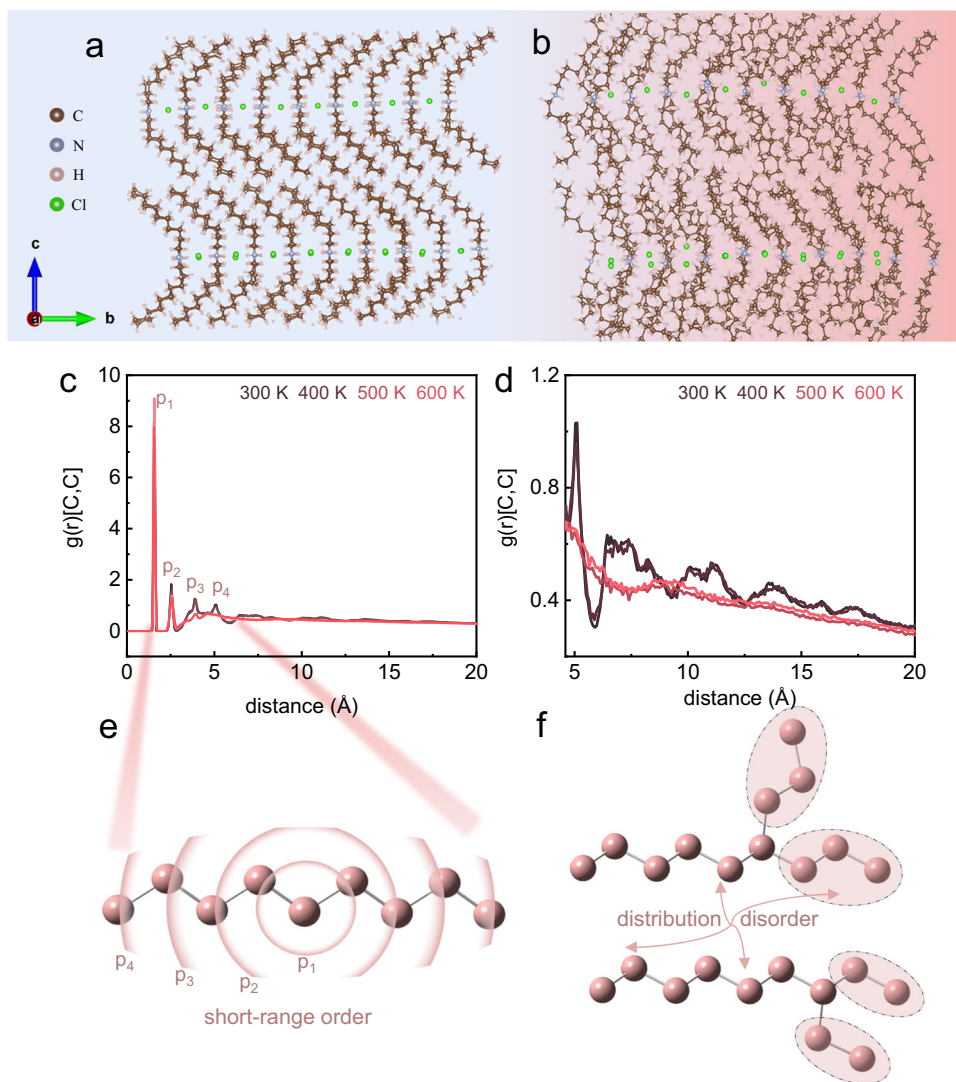


Fig. 6 | MD simulation on the $(\text{CH}_3-(\text{CH}_2)_9)_2\text{NH}_2\text{Cl}$. MD results of molecular crystal structure are shown in (a) for 300 K and (b) for 500 K. c The radial distribution function of carbon atoms at variable temperatures in the range of 0–20 Å.

d Enlarged zone of 5–20 Å from (c). e The schematic demonstration of short-range order of carbon chain. f The schematic demonstration of distribution disorder of carbon chain at long-range level.

molecular vibration modes occurs across the LTS–HTS phase transition at 323–326 K, which is in accordance with the DSC and XRD results. The vibration modes on NH_2 , CH_2 and CH_3 groups along the entire organic chains (Fig. 8a) are elaborated below.

For the NH_2 group at the center of $(\text{CH}_3-(\text{CH}_2)_9)_2\text{NH}_2^+$ (Fig. 8a), the N–H symmetric and asymmetric bending vibrations appear in the range of $1500\text{--}1600\text{ cm}^{-1}$ ^{45,46}. As shown in Fig. 8b, at LTS, the NH_2^+ bending mode is split at three frequencies of 1593 cm^{-1} , 1559 cm^{-1} and 1541 cm^{-1} , which is due to the different length of N–H...Cl hydrogen bonds (consistent with the SC-XRD result in Supplementary Table S5). Across the LTS–HTS transition, the intensity of bending vibrations with higher frequency at 1593 cm^{-1} enhances meanwhile the vibrations at 1541 cm^{-1} and 1559 cm^{-1} tend to disappear, which indicates the weakening of N–H...Cl hydrogen bonds and nonequivalent-equivalent environment change of hydrogen bonds during LTS–HTS phase transition. Moreover, as shown in Fig. 8e, N–H stretching modes appear at 2787 cm^{-1} and 2984 cm^{-1} at LTS⁴⁷, which get weakened across T_s , demonstrating the change of hydrogen bond environment during phase transition as well⁴⁷. In addition, at LTS, the dispersive broad absorption bands in the range of $2300\text{--}2600\text{ cm}^{-1}$ (Fig. 8d) can be assigned as NH_2^+ stretching vibrations with N–H...Cl hydrogen bond environment⁴⁸. The dynamic motion of NH_2^+ group result in the

continuously variable hydrogen bond interaction, which induces the variable N–H distance and consequently variable N–H stretching vibration frequencies; hence multiple bands appear successively at $2300\text{--}2600\text{ cm}^{-1}$ at LTS. At HTS, the intensity of dispersive NH_2^+ stretching bands gets decreased, indicating that the effect of hydrogen bond interaction on NH_2^+ group gets weakened across the phase transition.

As for the CH_2 group at the body of carbon chains (Fig. 8a), two bands at 1467 cm^{-1} and 1482 cm^{-1} are assigned to the C–H scissoring vibrations of CH_2 group at the LTS (Fig. 8b)⁴⁶, where the band splitting of C–H scissoring vibrations indicates the interchain vibrational coupling⁴⁶. With the LTS–HTS transition, the two bands suddenly merge into one with lower frequency (Fig. 8c), which indicates the interaction of intralayer chains get weakened⁴⁹.

Moreover, for the CH_3 group at the tail of carbon chains (Fig. 8a), C–H symmetric and asymmetric stretching vibration bands are assigned at 2869 cm^{-1} and 2953 cm^{-1} (Fig. 8e)⁴⁶, and their blueshift across T_s on heating indicates that the CH_3 group get less restricted and underlyingly vdW interaction between the carbon chains along their extension direction (c axis) becomes weak on heating; that is, the interlayer vdW interaction is weakened; also, the CH_3 umbrella deformation mode appears at 1376 cm^{-1} at LTS,

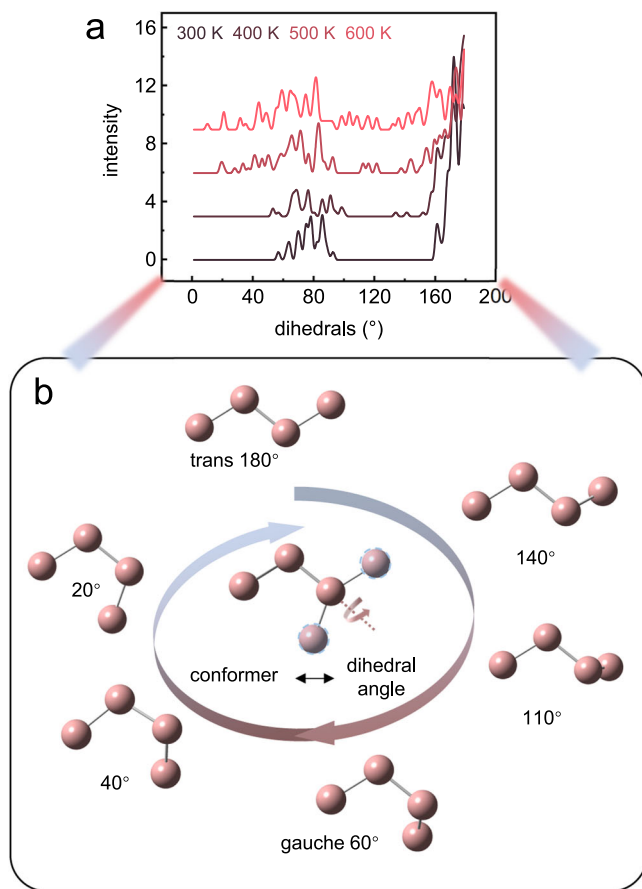


Fig. 7 | The distribution of C–C–C dihedral angle composed of 3 C–C bonds from the MD simulation for $(\text{CH}_3-(\text{CH}_2)_9)_2\text{NH}_2\text{Cl}$. **a** The dihedral angle distribution at variable temperatures. **b** The schematic relation between the carbon chain conformer and the dihedral angle.

shifting to 1379 cm^{-1} at HTS (Fig. 8b, c) due to the effect of interlayer interaction weakening⁴⁶. All these are in accordance with the effect caused by the extraordinary enlargement of interlayer spacing along *c* axis (Fig. 5d).

Overall, undergoing the LTS-HTS transition, the intralayer N–H...Cl hydrogen bond interaction gets weakened, which renders the freer motion of ammonium polar head (NH_2^+), also the intralayer and interlayer vdW interaction between carbon chains gets weakened across the phase transition, accounting for the disordered conformations of organic chains with less hindrance at HTS and the colossal entropy change of phase transition. Furthermore, the significantly weakening interlayer vdW interaction through CH_3 group specifically gives rise to the extraordinary expansion of interlayer spacing along *c* axis, critically leading to the large volume change of phase transition in such 2D alkylammonium halide, which accords well with the PXRD results shown in Fig. 5.

Discussion

Conventional 3D plastic crystals enable intensive orientational disorder of molecules at plastic crystalline state, which is favored by the high symmetry of relatively small molecule and cubic lattice⁵⁰. Although producing colossal entropy change from molecular orientational order-disorder transition, the 3D plastic crystals exhibit relatively limited volume change across the phase transition and considerable incompatibility of ordered crystalline and plastic crystalline structures, which generally induces large hysteresis in most 3D plastic crystals²³ (Table 1). Therefore, the characteristics of large

entropy change, large hysteresis and relatively limited volume expansion contribute to low pressure-sensitivity and large pressure hysteresis of phase transition, hindering the colossal caloric effect reversibly driven by low pressure in 3D plastic crystals. After introducing the long alkyl chains in 3D plastic crystals, as for the resulted 2D vdW dialkylammonium halide $(\text{CH}_3-(\text{CH}_2)_9)_2\text{NH}_2\text{Cl}$ in this work, the alignment of long carbon chains constructs the anisotropic interaction in crystal, involving strong intralayer hydrogen bond perpendicular to the direction of chain extension and weak interlayer vdW force along the direction of chain extension. Leveraging the 2D character, there forms the phase transition during which interlayer vdW interactions get significantly weakened and interlayer spacing significantly enlarges, hence drastic orientational disorder of partial group emerges in long $((\text{CH}_3-(\text{CH}_2)_9)_2\text{NH}_2)^+$ chains, i.e., conformational disorder of organic chains; consequently, the colossal entropy change and large volume change of phase transition can be realized altogether. Also, the interlayer weak vdW force-related 2D structural feature is deduced to induce low energy barrier of phase transition and consequently low hysteresis, for instance the hysteresis lower than 10 K in present dialkylammonium halide system and the hysteresis lower than 5 K in hybrid organic–inorganic layered perovskites^{28,29}. Therefore, the combination of large entropy change, large volume change-related high pressure-sensitivity and weak vdW force-related low hysteresis of phase transition contributes to the enhanced reversibility of BCE meanwhile maintaining the advantage of colossal thermal effect in 3D plastic crystals, accomplishing the colossal reversible BCE driven by low pressure in 2D vdW alkylammonium halides.

To conclude, leveraging quasi-direct and direct barocaloric measurement, we report the reversible colossal barocaloric effect in the 2D vdW dialkylammonium halides $(\text{CH}_3-(\text{CH}_2)_{n-1})_2\text{NH}_2\text{X}$ (X: halogen element). The reversible entropy change attains to $\Delta S_r \sim 400\text{ J kg}^{-1}\text{ K}^{-1}$ while the directly measured adiabatic temperature change reaches $\Delta T_{\text{ad}} \sim 11\text{ K}$ under a pressure lower than 0.1 GPa in the representative $(\text{CH}_3-(\text{CH}_2)_9)_2\text{NH}_2\text{Cl}$, surpassing all other reported barocaloric materials. Combining SC-XRD, PXRD, MD simulations with IR spectra analysis, the colossal thermal effect is indicated to stem from a phase transition with dramatic order-disorder conformation change of organic chains within the 2D layered structure. Across the phase transition, the prominent weakening of interlayer vdW interactions along extension direction of carbon chains (*c* axis) induces the significantly enlarged volume ($\Delta V/V \sim 12\%$; $\Delta c/c \sim 13\%$) for the accommodation of organic chains with sufficiently disordered conformation, rendering the large volume change, large entropy change and related low hysteresis of phase transition; ultimately, the colossal thermal effect can be driven reversibly by low pressure, generating the reversible colossal barocaloric effect. This work presents an emergent barocaloric mechanism available for the design strategy of barocaloric cooling refrigerant by constructing 2D vdW alkylammonium halides with long carbon chains cooperated.

Methods

Sample preparations

$(\text{CH}_3-(\text{CH}_2)_{n-1})_2\text{NH}_2\text{X}$ (X = Cl, Br) materials were synthesized by a reaction in anhydrous ethyl alcohol. The preparation process below produces polycrystal samples. Generally, the dialkylamine $((\text{C}_n\text{H}_{2n+1})_2\text{NH})$ and hydrochloric acid (mass fraction of 0.37) were weighed at a molar ratio of 1:1, and then added into the ethyl alcohol, the hydrochloric acid being added drop by drop. The mixture was heated and stirred under reflux for six hours, then on cooling, precipitate appears slowly. For purification, the product was recrystallized at least for three times with anhydrous ethyl alcohol.

Specifically, for cultivating single crystal of $(\text{CH}_3-(\text{CH}_2)_{n-1})_2\text{NH}_2\text{X}$ ($n=10$; X = Cl, Br) samples, recrystallization were conducted via

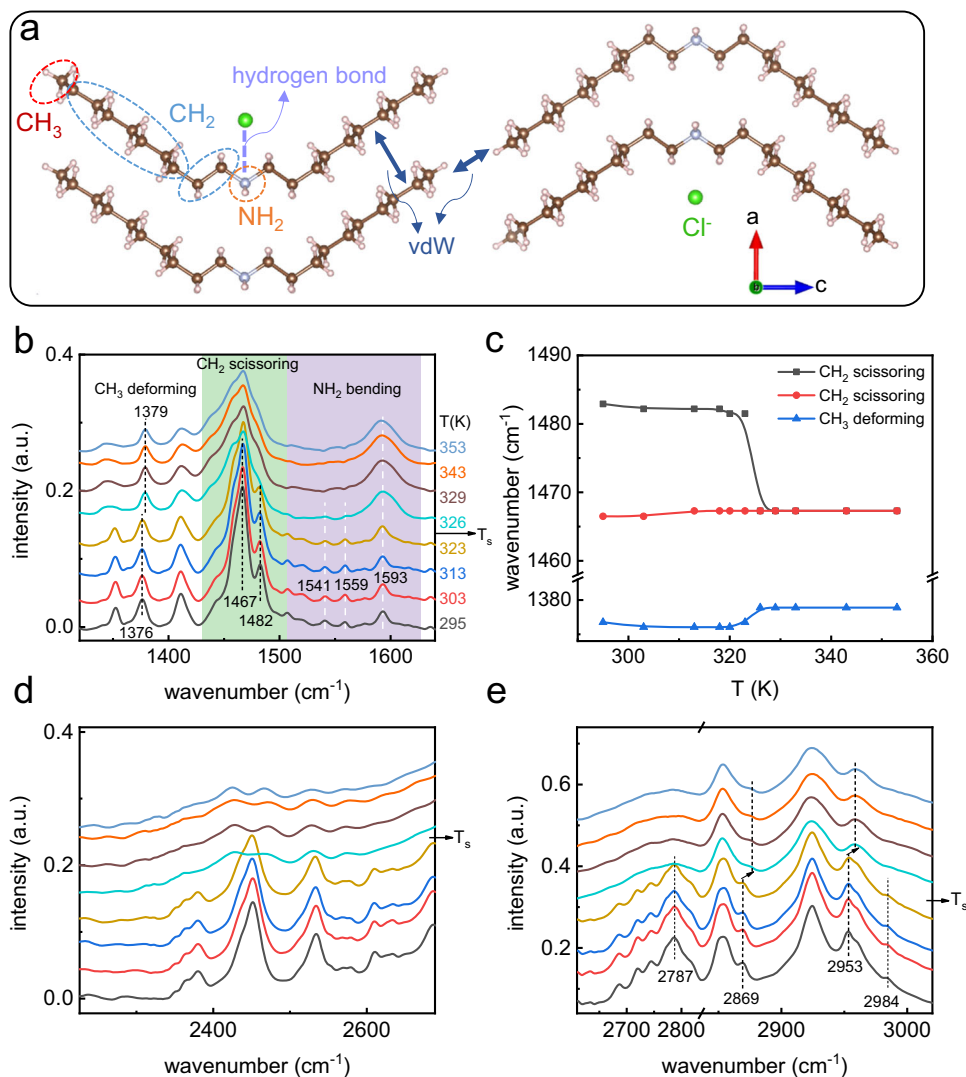


Fig. 8 | Temperature-variable infrared spectra of $(\text{CH}_3-(\text{CH}_2)_9)_2\text{NH}_2\text{Cl}$. **a** The interchain and interlayer vdW interactions and the hydrogen bond interaction of organic chains with Cl^- anions in $(\text{CH}_3-(\text{CH}_2)_9)_2\text{NH}_2\text{Cl}$. **b** Temperature-variable infrared spectra in the range of 1300–1650 cm^{-1} . **c** Temperature-

dependent vibration frequency of specific vibration band in **(b)**. **d, e** Temperature-variable infrared spectra in the range of 2300–2700 cm^{-1} and 2700–3000 cm^{-1} , respectively.

slow evaporation for one week without any motion and interference. Then high-quality single crystal of $(\text{CH}_3-(\text{CH}_2)_9)_2\text{NH}_2\text{Cl}$ and $(\text{CH}_3-(\text{CH}_2)_9)_2\text{NH}_2\text{Br}$ could be obtained.

High resolution single crystal x-ray diffraction (SC-XRD)

at variable temperatures was performed by BRUKER D8 VENTURE with $\lambda = 0.71073 \text{ \AA}$. The datasets of $(\text{CH}_3-(\text{CH}_2)_9)_2\text{NH}_2\text{Cl}$ were collected on heating using the Multi-Scan method (SADABS). The structure was solved and refined using the Bruker SHELXTL Software Package.

Powder x-ray diffraction (PXRD)

at variable temperatures was measured by Rigaku Smartlab using Cu $K\alpha$ radiation. The structure of low-temperature-state was refined by Rietveld method using the General Structure Analysis System (GSAS) suite, while the lattice parameters of high-temperature-state was obtained by Le bail method using the GSAS suite.

Pressure differential scanning calorimetry (P-DSC)

was used to characterize barocaloric effect by measuring heat flow under pressure. The pressure μDSC7 evo microcalorimeter (SETARAM,

France) was employed, which provides pressure 0–0.1 GPa by compressed N_2 gas with high purity (99.999%).

Infrared (IR) spectra

were measured using a BRUKER TENSOR II FTIR (Fourier Transform Infrared) spectrometer in the frequency range of 900–4000 cm^{-1} with 1.5 cm^{-1} resolution.

The classic molecular dynamics (MD) simulations

were performed using the LAMMPS package with periodic boundary condition⁵¹. The reactive force field (ReaxFF) was utilized in our MD simulations⁵². The Newton equation of motion was integrated by the velocity Verlet algorithm and the time-step is 0.5 fs. Based on the lattice parameters from SC-XRD at 300 K for $(\text{CH}_3-(\text{CH}_2)_9)_2\text{NH}_2\text{Cl}$, we constructed a 8^*8^*2 supercell at low-temperature-state. MD simulations were performed by heating the supercell from 1 K to 800 K in the NPT ensemble (3,000,000 time steps), then tracking the supercell structure at variable temperature for low-temperature-state and high-temperature-state. The radial distribution function and dihedral angle distribution are obtained via I.S.A.A.C.S. (Interactive Structure Analysis of Amorphous and Crystalline Systems) on the MD results.

Direct measurement of adiabatic temperature change ΔT_{ad} driven by pressure

The quasi-adiabatic condition was constructed by an isothermal bath combined with the fast operation of pressurization and depressurization. At constant temperatures set by isothermal bath, the sample containing K-type thermocouple was pressurized up to set point within 3 s, then ΔT_{ad} induced by pressurization can be measured; however the target pressure cannot be fully maintained but spontaneously release some due to our device, then the sample decreased to bath temperature for the thermal equilibrium with environment; after sample kept at bath temperature, the remained pressure was released within 3 s, then the underestimated ΔT_{ad} induced by depressurization can be obtained. Through several pressurization-depressurization cycles, the reversible adiabatic temperature change (ΔT_r) at bath temperature can be obtained. The schematic diagram for directly measuring ΔT_{ad} is shown in Fig. 4d.

Calculation of barocaloric entropy change and adiabatic temperature change

Based on the heat flow (Q) response of temperature at variable pressure, the phase transition entropy curves can be constructed via the integration of heat flow⁵³:

$$S_{pt}(T, P) = \int_{T_0}^T \frac{1}{T'} \frac{Q(T', P)}{dT'} dT' \quad (1)$$

Considering the thermal response besides the latent heat of phase transition, the total entropy curves can be constructed including the specific heat capacity contribution, where specific heat capacity C_p at variable pressures were approximated as that for atmosphere pressure:

$$S(T, P) = S_{pt}(T, P) + \int_{T_0}^T \frac{C_p}{T'} dT' \quad (2)$$

Isothermal entropy change curves (ΔS_p) can be obtained quasi-directly by isothermal subtraction of entropy curves at variable pressure: $\Delta S_p(T, P_0 \rightarrow P_1) = S(T, P_1) - S(T, P_0)$. Concretely, the ΔS_p for pressurization process ($P_0 < P_1$) utilizes the Q(T, P) on cooling, while the ΔS_p for depressurization ($P_0 > P_1$) process utilizes the Q(T, P) on heating. And reversible isothermal entropy change ΔS_r can be treated as the overlapping of ΔS_p between pressurization and depressurization processes.

Adiabatic temperature change curves (ΔT_p) can be obtained quasi-directly by adiabatic subtraction of entropy curves at variable pressure: $\Delta T_p(T, P_0 \rightarrow P_1) = T(S, P_1) - T(S, P_0)$. Similar to ΔS_p , the ΔT_p for pressurization process should be decided by entropy curves on cooling, while the ΔT_p for depressurization process be decided by entropy curves on heating. Reversible adiabatic temperature change ΔT_r can be obtained by the adiabatic subtraction of heating entropy curve at atmosphere pressure and cooling entropy curve at applied pressure⁵⁴.

Data availability

The main data supporting the findings of this study are available within the paper and its Supplementary Information. Considering the huge quantity of raw data, all raw data generated during the current study are available from the corresponding author (F.X.H.) upon request.

References

- Moya, X. & Mathur, N. D. Caloric materials for cooling and heating. *Science* **370**, 797–803 (2020).
- Pecharsky, V. K. & Gschneidner, K. A. Jr. Giant magnetocaloric effect in $Gd_5(Si_2Ge_2)$. *Phys. Rev. Lett.* **78**, 4494–4497 (1997).
- Hu, F. et al. Influence of negative lattice expansion and metamagnetic transition on magnetic entropy change in the compound $LaFe_{11.4}Si_{1.6}$. *Appl. Phys. Lett.* **78**, 3675–3677 (2001).
- Tegus, O., Brück, E., Buschow, K. H. J. & De Boer, F. R. Transition-metal-based magnetic refrigerants for room-temperature applications. *Nature* **415**, 150–152 (2002).
- Law, J. Y. et al. A quantitative criterion for determining the order of magnetic phase transitions using the magnetocaloric effect. *Nat. Commun.* **9**, 2680 (2018).
- Mischenko, A. S., Zhang, Q., Scott, J. F., Whatmore, R. W. & Mathur, N. D. Giant electrocaloric effect in thin-film $PbZr_{0.95}Ti_{0.05}O_3$. *Science* **311**, 1270–1271 (2006).
- Ma, R. et al. Highly efficient electrocaloric cooling with electrostatic actuation. *Science* **357**, 1130–1134 (2017).
- Bonnot, E., Romero, R., Mañosa, L., Vives, E. & Planes, A. Elastocaloric effect associated with the martensitic transition in shape-memory alloys. *Phys. Rev. Lett.* **100**, 125901 (2008).
- Tušek, J. et al. A regenerative elastocaloric heat pump. *Nat. Energy* **1**, 16134 (2016).
- Lloveras, P. & Tamarit, J.-L. Advances and obstacles in pressure-driven solid-state cooling: a review of barocaloric materials. *MRS Energy Sustain.* **8**, 3–15 (2021).
- Aznar, A. et al. Giant and reversible inverse barocaloric effects near room temperature in ferromagnetic $MnCoGeB_{0.03}$. *Adv. Mater.* **31**, 1903577 (2019).
- Stern-Taulats, E. et al. Barocaloric and magnetocaloric effects in $Fe_{49}Rh_{51}$. *Phys. Rev. B* **89**, 214105 (2014).
- Mañosa, L. et al. Giant solid-state barocaloric effect in the Ni–Mn–In magnetic shape-memory alloy. *Nat. Mater.* **9**, 478–481 (2010).
- Mañosa, L. et al. Inverse barocaloric effect in the giant magnetocaloric La–Fe–Si–Co compound. *Nat. Commun.* **2**, 595 (2011).
- Mañosa, L. et al. Barocaloric effect in metamagnetic shape memory alloys: barocaloric effect in memory alloys. *Phys. Status Solidi B* **251**, 2114–2119 (2014).
- Matsunami, D., Fujita, A., Takenaka, K. & Kano, M. Giant barocaloric effect enhanced by the frustration of the antiferromagnetic phase in Mn_3GaN . *Nat. Mater.* **14**, 73–78 (2015).
- Stern-Taulats, E. et al. Tailoring barocaloric and magnetocaloric properties in low-hysteresis magnetic shape memory alloys. *Acta Mater.* **96**, 324–332 (2015).
- Yuce, S. et al. Barocaloric effect in the magnetocaloric prototype $Gd_5Si_2Ge_2$. *Appl. Phys. Lett.* **101**, 071906 (2012).
- Wu, R.-R. et al. Giant barocaloric effect in hexagonal Ni_2In -type Mn–Co–Ge–In compounds around room temperature. *Sci. Rep.* **5**, 18027 (2015).
- Li, B. et al. Colossal barocaloric effects in plastic crystals. *Nature* **567**, 506–510 (2019).
- Lloveras, P. et al. Colossal barocaloric effects near room temperature in plastic crystals of neopentylglycol. *Nat. Commun.* **10**, 1803 (2019).
- Cazorla, C. & Errandonea, D. Giant mechanocaloric effects in fluorite-structured superionic materials. *Nano Lett.* **16**, 3124–3129 (2016).
- Aznar, A. et al. Reversible and irreversible colossal barocaloric effects in plastic crystals. *J. Mater. Chem. A* **8**, 639–647 (2020).
- Yoshida, Y., Yuse, K., Guyomar, D., Capsal, J.-F. & Sebald, G. Elastocaloric effect in poly(vinylidene fluoride-trifluoroethylene-chlorotrifluoroethylene) terpolymer. *Appl. Phys. Lett.* **108**, 242904 (2016).
- Aznar, A. et al. Reversible colossal barocaloric effects near room temperature in 1-X-adamantane (X=Cl, Br) plastic crystals. *Appl. Mater. Today* **23**, 101023 (2021).
- Romanini, M. et al. Giant and reversible barocaloric effect in trinuclear spin-crossover complex $Fe_3(bntrz)_6(tcnsct)_6$. *Adv. Mater.* **33**, 2008076 (2021).
- Li, J. et al. Colossal reversible barocaloric effects in layered hybrid perovskite $(C_{10}H_{21}NH_3)_2MnCl_4$ under low pressure near room temperature. *Adv. Funct. Mater.* **31**, 2105154 (2021).
- Gao, Y. et al. Reversible colossal barocaloric effect dominated by disordering of organic chains in $(CH_3-(CH_2)_{n-1}-NH_3)_2MnCl_4$ single crystals. *NPG Asia Mater.* **14**, 34 (2022).

29. Seo, J. et al. Colossal barocaloric effects with ultralow hysteresis in two-dimensional metal-halide perovskites. *Nat. Commun.* **13**, 2536 (2022).
30. Li, F. B. et al. Understanding colossal barocaloric effects in plastic crystals. *Nat. Commun.* **11**, 4190 (2020).
31. Cui, J. et al. Combinatorial search of thermoelastic shape-memory alloys with extremely small hysteresis width. *Nat. Mater.* **5**, 286–290 (2006).
32. Zarnetta, R. et al. Identification of quaternary shape memory alloys with near-zero thermal hysteresis and unprecedented functional stability. *Adv. Funct. Mater.* **20**, 1917–1923 (2010).
33. Liang, Y. G. et al. Tuning the hysteresis of a metal-insulator transition via lattice compatibility. *Nat. Commun.* **11**, 3539 (2020).
34. Das, S., Mondal, A. & Reddy, C. M. Harnessing molecular rotations in plastic crystals: a holistic view for crystal engineering of adaptive soft materials. *Chem. Soc. Rev.* **49**, 8878–8896 (2020).
35. Brand, R., Lunkenheimer, P. & Loidl, A. Relaxation dynamics in plastic crystals. *J. Chem. Phys.* **116**, 10386–10401 (2002).
36. Luo, J. et al. 1,2,4-Triazolium perfluorobutanesulfonate as an archetypal pure protic organic ionic plastic crystal electrolyte for all-solid-state fuel cells. *Energy Environ. Sci.* **8**, 1276–1291 (2015).
37. van Oort, M. J. M. & White, M. A. Polymorphism in dialkylammonium chlorides. An adiabatic calorimetry study. *Ber. Bunsenges. Phys. Chem.* **92**, 168–176 (1988).
38. Whitman, C. A., Johnson, M. B. & White, M. A. Characterization of thermal performance of a solid–solid phase change material, di-*n*-hexylammonium bromide, for potential integration in building materials. *Thermochim. Acta* **531**, 54–59 (2012).
39. Steinert, S., Voigt, W., Glausch, R. & Neuschütz, M. Thermal characteristics of solid–solid phase transitions in long-chain dialkyl ammonium salts. *Thermochim. Acta* **435**, 28–33 (2005).
40. Le Bail, A. Whole powder pattern decomposition methods and applications: a retrospection. *Powder Diffr.* **20**, 316–326 (2005).
41. Alfè, D., Cazorla, C. & Gillan, M. J. The kinetics of homogeneous melting beyond the limit of superheating. *J. Chem. Phys.* **135**, 024102 (2011).
42. Przygocki, W. Radial distribution function in polymers. in *Proc. SPIE* **3095**, 92–102 (1997).
43. Lin, J. et al. Colossal and reversible barocaloric effect in liquid–solid-transition materials *n*-alkanes. *Nat. Commun.* **13**, 596 (2022).
44. Domalski, E. S. & Hearing, E. D. Heat capacities and entropies of organic compounds in the condensed phase. Volume III. *J. Phys. Chem. Ref. Data* **25**, 1 (1996).
45. Casal, H. L., Mantsch, H. H. & Cameron, D. G. An infrared spectroscopic study of the structural phase transition of *n*-C₁₀H₂₁NH₃Cl. *Solid State Commun.* **49**, 571–573 (1984).
46. Wei, W., Laiming, L. & Shiquan, X. An infrared spectroscopic characterization of the solid–solid behavior of dodecylammonium chloride. *J. Phys. Chem. Solids* **54**, 73–77 (1993).
47. Lindgren, J. & Arran, N. The crystal structure of a high temperature modification of dimethylammonium chloride (CH₃)₂NH₂Cl: an x-ray and infrared Study. *Acta Chem. Scand.* **26**, 3043–3052 (1972).
48. Weng, S. *Fourier transform infrared spectral analysis*. (Beijing: Chemical Industry Press, 2010).
49. Vaia, R. A., Teukolsky, R. K. & Giannelis, E. P. Interlayer structure and molecular environment of alkylammonium layered silicates. *Chem. Mater.* **6**, 1017–1022 (1994).
50. Timmermans, P. J. Plastic crystals: a historical review. *J. Phys. Chem. Solids* **18**, 1–8 (1961).
51. Plimpton, S. Fast parallel algorithms for short-range molecular dynamics. *J. Comput. Phys.* **117**, 1–19 (1995).
52. Ganeshan, K. et al. Structure and dynamics of aqueous electrolytes confined in 2D-TiO₂/Ti₃C₂T₂ MXene Heterostructures. *ACS Appl. Mater. Interfaces* **12**, 58378–58389 (2020).
53. Moya, X., Kar-Narayan, S. & Mathur, N. D. Caloric materials near ferroic phase transitions. *Nat. Mater.* **13**, 439–450 (2014).
54. Aznar, A. et al. Giant barocaloric effects over a wide temperature range in superionic conductor AgI. *Nat. Commun.* **8**, 1851 (2017).
55. Tamarit, J. Li., Legendre, B. & Buisine, J. M. Thermodynamic study of some neopentane derived by thermobarometric analysis. *Mol. Cryst. Liq. Cryst.* **250**, 347–358 (1994).
56. Eilerman, D. & Rudman, R. Polymorphism of crystalline poly(-hydroxymethyl) compounds. III. The structures of crystalline and plastic tris(hydroxymethyl)aminomethane. *J. Chem. Phys.* **72**, 5656–5666 (1980).
57. Salvatori, A. et al. Colossal barocaloric effects in adamantane derivatives for thermal management. *APL Mater.* **10**, 111117 (2022).
58. Yu, Z. et al. Colossal barocaloric effect achieved by exploiting the amorphous high entropy of solidified polyethylene glycol. *NPG Asia Mater.* **14**, 96 (2022).
59. Zhang, Z. et al. Thermal batteries based on inverse barocaloric effects. *Sci. Adv.* **9**, eadd0374 (2023).

Acknowledgements

This work was supported by the Science Center of the National Science Foundation of China (52088101(B.-G.S.)), the National Key Research and Development Program of China (2021YFB3501202 (F.-X.H.), 2020YFA0711500 (J.W.), 2019YFA0704900 (F.-X.H.), 2022YFB3505201 (J.W.), 2021YFA1400300 (B.-G.S.), 2023YFA1406003 (F.-X.H.)), the National Natural Sciences Foundation of China (92263202 (F.-X.H.), U23A20550 (F.-X.H.), 22361132534 (J.W.), 51971240 (J.W.)), the Strategic Priority Research Program B (XDB33030200 (B.-G.S.)) of Chinese Academy of Sciences (CAS), and the Synergetic Extreme Condition User Facility (SECUF). The authors acknowledge Dr. Yan Chen (North China Electric Power University, Beijing 102206, China) for her help during the RDG calculation.

Author contributions

F.X.H. and B.G.S. formulated the project. Y.H.G. synthesized the compounds. Y.H.G., Q.Z.H., Z.Y.T. and B.J.W. collected and analyzed the powder x-ray diffraction data. Y.H.G. and Y.T.S. collected and analyzed single-crystal x-ray diffraction data. Y.H.G. collected and analyzed the pressure calorimetry data. Y.H.G., Z.B.Y., H.B.Z. and Y.K. collected the adiabatic temperature data from the direct measurement. Y.H.G. and S.K.Y. collected and analyzed the infrared data. D.H.W. and Y.H.G. did the molecular dynamics simulation with help of Y.L.L., J.W. and Y.Liu. Y.H.G. analyzed the simulation results. Y.H.G. and F.X.H. wrote the paper with input from all coauthors. Y.Lin, Y.Z.C., J.R.S. and T.Y.Z. contributed to discussing and revising the paper.

Competing interests

The authors declare no competing interests.

Additional information

Supplementary information The online version contains supplementary material available at <https://doi.org/10.1038/s41467-024-46248-1>.

Correspondence and requests for materials should be addressed to Feng-Xia Hu, Jing Wang, Yun-liang Li or Bao-Gen Shen.

Peer review information *Nature Communications* thanks the anonymous reviewer(s) for their contribution to the peer review of this work. A peer review file is available.

Reprints and permissions information is available at <http://www.nature.com/reprints>

Publisher's note Springer Nature remains neutral with regard to jurisdictional claims in published maps and institutional affiliations.

Open Access This article is licensed under a Creative Commons Attribution 4.0 International License, which permits use, sharing, adaptation, distribution and reproduction in any medium or format, as long as you give appropriate credit to the original author(s) and the source, provide a link to the Creative Commons licence, and indicate if changes were made. The images or other third party material in this article are included in the article's Creative Commons licence, unless indicated otherwise in a credit line to the material. If material is not included in the article's Creative Commons licence and your intended use is not permitted by statutory regulation or exceeds the permitted use, you will need to obtain permission directly from the copyright holder. To view a copy of this licence, visit <http://creativecommons.org/licenses/by/4.0/>.

© The Author(s) 2024